COMMUNICATIONS CHEMISTRY

ARTICLE

https://doi.org/10.1038/s42004-019-0197-1 OPEN

Carboxylic acid induced near-surface restructuring of a magnetite surface

Björn Arndt[1,2,4], Kai Sellschopp[3,4], Marcus Creutzburg[1,2], Elin Grånäs[1], Konstantin Krausert[1,2], Vedran Vonk[1], Stefan Müller[3], Heshmat Noei[1], Gregor B.V. Feldbauer[3] & Andreas Stierle[1,2]

A fundamental knowledge of the interaction of carboxylic acids, such as formic acid, with magnetite surfaces is of prime importance for heterogeneous catalysis and the synthesis of novel materials. Despite this, little is known about the atomic scale adsorption mechanisms. Here we show by in-situ surface X-ray diffraction that the oxygen rich subsurface cation vacancy reconstruction of the clean magnetite (001) surface is lifted by dissociative formic acid adsorption, reestablishing a surface with bulk stoichiometry. Using density functional theory, the bulk terminated, fully formic acid covered surface is calculated to be more stable than the corresponding clean, reconstructed surface. A comparison of calculated and experimental infrared bands supports the bidentate adsorption geometry and a specific adsorption site. Our results pave the way for a fundamental understanding of the bonding mechanism at carboxylic acid/oxide interfaces.

[1] Deutsches Elektronen-Synchrotron (DESY), D-22607 Hamburg, Germany. [2] Fachbereich Physik Universität Hamburg, Jungiusstr. 9, 20355 Hamburg, Germany. [3] Institute of Advanced Ceramics, Hamburg University of Technology, Denickestr. 15, D-21073 Hamburg, Germany. [4] These authors contributed equally: Björn Arndt, Kai Sellschopp. Correspondence and requests for materials should be addressed to A.S. (email: andreas.stierle@desy.de)

The interaction of carboxylic acids with oxide surfaces is important for a variety of technological applications. Formic acid, as the smallest representative of carboxylic acid molecules, is discussed as a potential intermediate or byproduct in many reactions catalyzed by iron oxides[1], such as the water-gas shift reaction[2] or Fischer–Tropsch synthesis[3], which are both relevant for a future sustainable energy cycle. A fundamental knowledge of the interaction of carboxylic acids with oxide surfaces is also of prime importance in materials synthesis from well defined building blocks. Carboxylic acids, such as oleic acid, are widely employed during the wet chemical synthesis of oxide nanoparticles with tailored size and shape[4,5]. Oleic acid stabilized magnetite nanoparticles can be used as building blocks for hierarchical materials with exceptional bending modulus, hardness and strength[6,7].

Despite the relevance of oxide/carboxylic acid interfaces in different context, controlled adsorption studies are scarce. Various important fundamental questions concerning the adsorption geometry, structural and compositional changes at oxide surfaces induced by adsorption of carboxylic acids have not been answered to date[8,9]. A fundamental knowledge of the atomic structure of oxide/carboxlic acid interfaces is required for a deeper understanding of the adsorption energetics and thermodynamics, as well as possible intermediate steps involved in reactions and adsorption induced changes in the interfacial geometric and electronic structure. These serve as a basis for the theoretical prediction of reactions paths, as well as the mechanical properties of hierarchical materials.

In this context, formic acid adsorption on magnetite single crystal surfaces serves as a prototypical, well defined experiment. Formic acid acts as a simple probe molecule, which is representative for larger organic acids with the same carboxylic end group, such as oleic acid. The magnetite (001) surface is of particular interest since under ultra high vacuum (UHV) conditions it exhibits well controlled, characteristic defects consisting of surface tetrahedral interstitial Fe ions and subsurface octahedral vacancies, leading to an oxygen rich surface termination[10,11]. The defects are long range ordered with $\sqrt{2}\times\sqrt{2}$ R45° periodicity, referred to in the following as subsurface cation vacancy (SCV) reconstruction. Previously it was reported that room temperature adsorption of formic acid surprisingly lifts the SCV reconstruction and transforms the surface into an ordered (1×1) structure[12] without providing further information on the reconstruction lifting mechanism itself. Based on infrared reflection absorption spectroscopy (IRRAS) and scanning tunneling microscopy (STM) experiments, it was proposed that the molecules dissociate and adsorb in a bidentate configuration, in which both oxygen atoms bind to two octahedrally coordinated surface Fe cations. A maximum coverage of two formic acid molecules per $\sqrt{2}\times\sqrt{2}$ R45° surface unit cell was identified by STM with two possible adsorption sites. It remained however unclear, which of the sites was preferentially occupied. It was also reported that the SCV reconstruction is lifted upon exposure to atomic hydrogen[13]; however, its lifting upon water exposure is discussed controversially in the literature[14–16].

Here, we present a combined surface X-ray diffraction (SXRD) and density functional theory (DFT) study of the atomic structure of the magnetite (001)/formic acid interface. This combination of methods is especially suited to address adsorption induced structural changes in the near surface region. We address important, open questions concerning the adsorption geometry, the atomic structure and stoichiometry in the near surface region, as well as the reconstruction lifting process. The calculated infrared spectra further underpin the interpretation of the experimental Fourier transform infrared reflection absorption spectroscopy (FT-IRRAS) spectra and are in line with the identification of one preferential formic acid adsorption site. First, we will discuss the experimental results, before presenting the theoretical analysis and summarizing both. Afterwards we will present the experimental and computational approach.

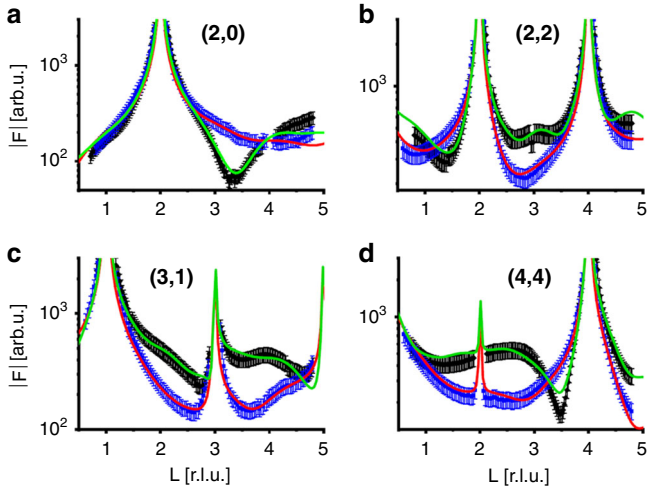

Fig. 1 Comparison of SXRD data before and after formic acid dosing. Clean surface SXRD structure factor magnitude *F* (black squares) and after dosing 50 L formic acid (blue squares). Also included is the best fit to the 50 L data set (red line) and to the clean surface data (green line). **a** (2, 0) rod, (**b**) (2, 2) rod, (**c**) (3, 1) rod, (**d**) (4, 4) rod

Results

Formic acid adsorption site determination. X-ray diffraction data were recorded and analyzed, after preparation of the sample surface, both as described in the methods section. As a first step, a reference SXRD data set of the clean, SCV reconstructed surface was recorded under UHV conditions at room temperature, see Fig. 1. The data confirm the recently established structural model for the SCV reconstruction[10,11], see Fig. 2a and Supplementary Table 1 for the atomic positions. In the [001]-direction, bulk magnetite is built up by layers of octahedrally coordinated iron and oxygen ions followed by tetrahedrally coordinated iron ion layers. In the SCV model one additional, interstitial tetrahedral iron atom is present per unit cell in the layer directly underneath the surface, which is terminated by a layer of octahedrally coordinated iron and oxygen. In addition, two octahedral iron vacancies are present in the second octahedral iron ion layer directly underneath. Therefore, one net iron ion is missing in the surface, as compared to a bulk termination with ideal Fe_3O_4 stoichiometry. This characteristic interstitial/vacancy configuration is accompanied by distortions in the crystal lattice, leading to a slight undulation of the iron-oxygen rows at the surface.

During dosing of formic acid at room temperature (see methods section for details), X-ray diffraction signals of a rod arising from the SCV reconstruction superstructure and a crystal truncation rod were monitored, see Supplementary Fig. 1. The (2, 1) peak of the reconstruction decreased by 90% upon exposure to 10 L formic acid. After nominally 50 L formic acid exposure, the reconstruction was found to be completely lifted based on the absence of any superstructure signal. At the same time, the crystal truncation rod (CTR) intensity at (2, 2, 1.6) increased by a factor of ~10, indicating strong interfacial structural rearrangements. The CTRs collected after fully lifting the reconstruction (see Fig. 1 and Supplementary Fig. 2 for the full data set) exhibit a shape very similar to that of a bulk truncated surface, in line with

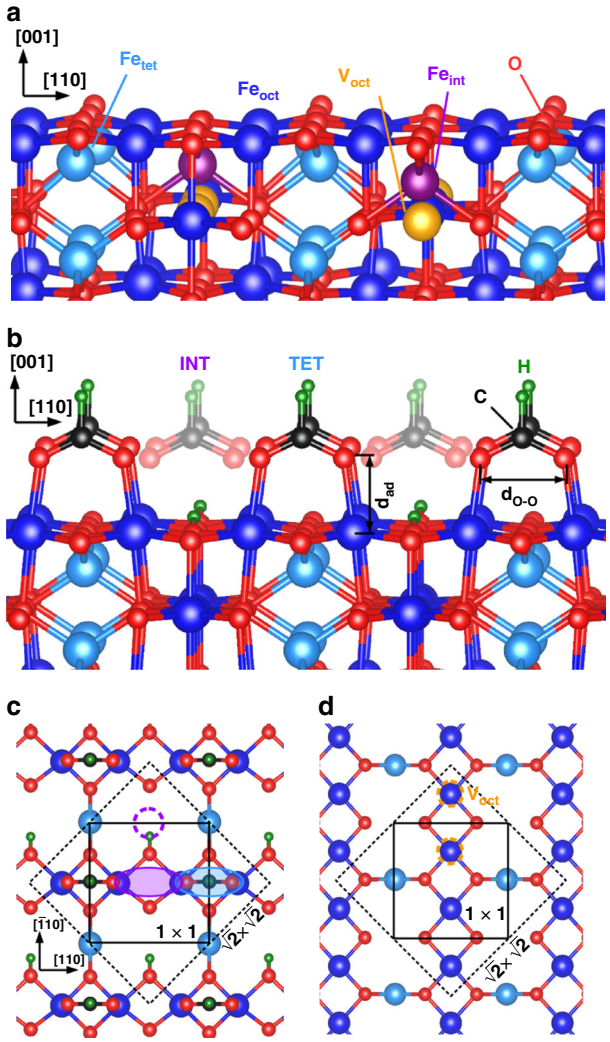

Fig. 2 Adsorption geometry of formic acid on Fe_3O_4(001). **a** Atomic structure of the clean, SCV reconstructed Fe_3O_4(001) surface (side view), oxygen atoms are plotted in red, tetrahedrally coordinated Fe ions in light blue, octahedrally coordinated Fe ions Fe_{oct} in dark blue, tetrahedrally coordinated interstitial Fe ions in purple, Fe ion vacancies in yellow, hydrogen atoms in green and carbon atoms in black. **b** bulk truncated surface structure with bidentate formic acid adsorption at the "tet" site (side view, "int" site also shown). The first and second layer of the surface unit cell are depicted in **c**, **d**, respectively (top view). For the reconstructed surface in the first layer every second tetrahedral "int" Fe site (dashed circle) is filled and the underlying two octahedral Fe sites in the second layer are vacant (V_{oct}), dashed circles in **d**

substantial changes in the atomic structure at and near the surface.

A full quantitative structural analysis was performed by fitting multiple models to the data. This included fits with formate only in one of the two different possible bidentate adsorption sites, as well as both of them (see Fig. 2b). In the "int" site, the formic acid molecule sits between two regular tetrahedrally coordinated Fe ions, whereas in the "tet" site, the molecule is located between two vacant tetrahedral sites of the unreconstructed surface, see Fig. 2b, c. Furthermore, different fits were performed, including the positions of the lattice iron ions only, the positions of both oxygen and iron ions, as well as occupation parameters for the additional interstitial tetrahedral iron sites, octahedral vacancies from the reconstruction, and of the surrounding iron atoms on regular lattice sites. Iron on interstitial subsurface sites was also included in the fits to account for the possibility of reorganization and diffusion of cations in the near-surface region. The occupation parameters for the octahedral iron atoms in the first layer were kept fixed since no vacancies on these positions were reported from the STM measurements[12]. As initial position for the adsorbed molecules the known adsorption geometry of formic acid on rutile TiO_2(110) was chosen, since it exhibits similar adsorption sites as magnetite (001)[17]. Because the in-plane distance of two adjacent octahedral iron ions in magnetite is larger (2.97 Å) than that between the oxygen atoms (2.21 Å) in formic acid, these oxygen atoms are not directly placed on top of the octahedral iron atoms, see Fig. 2b. Finally, a full refinement without including formate was performed to check the sensitivity of the fitting to these species. Since the result of this refinement was significantly worse ($\chi^2 = 0.95$) than that one including the formate ($\chi^2 = 0.63$) and led to unphysical positions of the oxygen atoms, we conclude that the fitting procedure is sensitive to the adsorbed formates. The surface structure with adsorbed formates is shown in Fig. 2b–d. Interestingly, there is a clear preference in the fits for formate adsorbed at the "tet" site (see Fig. 2), with an occupancy of 75 ± 10%, while the "int" site exhibits an occupancy of only 10 ± 10%. This is also found in the difference on the goodness-of-fit (χ^2_{red})-values for models with formate in only one of the two possible positions summarized in Table 1, and is also consistent with the DFT results as described below. Vacant sites (~15 ± 10%) are possibly present at the domain boundaries of molecules in different adsorption sites[12].

Formic acid induced near surface structure and composition. Next, we will discuss formic acid adsorption induced structural changes in the Fe_3O_4 substrate. All atoms were found to relax to positions close to their respective bulk positions upon lifting of the reconstruction, which implicates relaxations up to 0.31 Å for the oxygen ions at the surface and up to 0.28 Å for the iron ions[10]. Differences from the bulk positions occur mostly in the first layer of the unit cell, where, induced by the adsorbed formate, the surface iron ions are displaced outward by 0.060 ± 0.006 Å. In the in-plane direction they move towards the oxygen atoms of the formate in the tet-position by 0.094 ± 0.008 Å with respect to the bulk positions, while the adjacent oxygen atoms exhibit an inward displacement. Displacements in layers below the surface are between 0.002 and 0.02 Å and no significant differences from the bulk positions were found below the first three double layers. Supplementary Table 2 summarizes the atomic positions in comparison to the DFT results. Very similar trends were observed in the quantitative analysis of the data collected after 10 L formic acid adsorption, see Supplementary Fig. 3, Supplementary Tables 3 and 4, as well as Supplementary Note 1.

In the following, we will address the formic acid adsorption induced changes in the near surface occupation parameters. The crystal truncation rod measurements are very sensitive to the different sublattice cation occupancies, as we demonstrated for the reconstructed surface[11]. The interstitial tetrahedral site, fully occupied for the SCV reconstruction, shows for the best fit to the data a residual occupation of 9 ± 6%, while the octahedral vacancies are filled to 90 ± 3% (see solid red line in Fig. 1). In addition, none of the regular, adjacent iron sites was found to be depleted. This implies that the bulk stoichiometry is recovered at ≈90% of the surface during the reconstruction lifting process, in good agreement with the occupation of 85 ± 10% of the formic acid bidentate sites. Likely, iron ions from the interstitial

Table 1 Overview over the level of agreement of different models with the SXRD data

Type	Formate occupation		χ^2_{red}
	int-position	tet-position	
Fit to data	0	1	0.67
	1	0	0.92
	0.1	0.75	0.63
DFT-calculations	0	1	1.89
	1	0	2.27

χ^2_{red} denotes the so-called goodness-of-fit[18]

tetrahedral site fill one of the subsurface octahedral vacancies. One additional iron atom is needed per unit cell at the surface to convert back to bulk stoichiometry. No iron on interstitial sites was found in the analysis of the data obtained from the clean reconstructed surface prior to dosing, excluding it as a major source of these additional iron ions. Since a spillover of iron from any adjacent sites is not supported by the data analysis, all other possible sources for the additional iron directly located at the surface can be ruled out. The only possible source of the additional iron is therefore diffusion from lower layers towards the surface at room temperature. This corresponds to the dissolution of one iron vacancy in the bulk by local site exchange, possibly assisted by the vacancy induced strain field. The DFT calculations presented in the next section will shed more light onto this aspect.

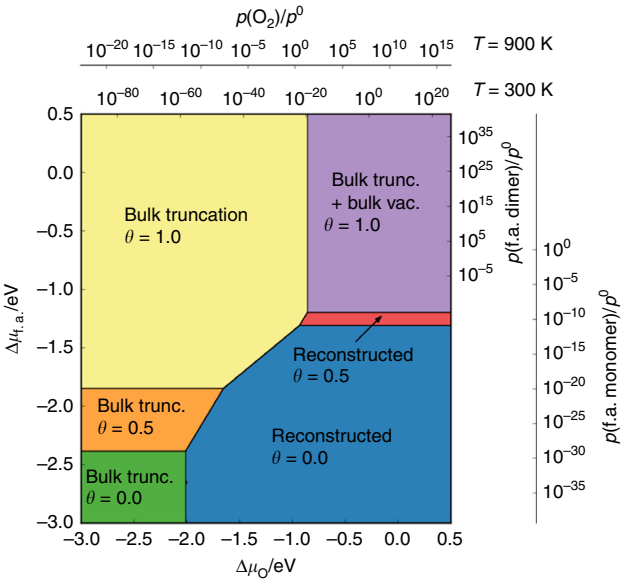

Fig. 3 Surface phase diagram of the Fe_3O_4(001) surface with exposure to oxygen and formic acid. The most stable surface structures for different thermodynamic conditions (chemical potential μ, pressure p with respect to atmospheric pressure $p^0 = 1$ bar) are shown, θ is the formic acid coverage of the corresponding structure. For oxygen the upper pressure scale is at 900 K and the lower scale is at 300 K. The scales for formic acid are at 300 K, but there is a transition from the monomer to the dimer configuration between 10^{-3} and 10^{-2} bar

Energetics of the reconstruction lifting. To get deeper insight in the mechanism and energetics of the reconstruction lifting on Fe_3O_4(001) upon adsorption of formic acid, total energy calculations based on density functional theory (DFT) were performed. The dissociative bidentate adsorption of formic acid on the SCV reconstructed Fe_3O_4(001) surface yields an adsorption energy of −1.19 eV per adsorbed molecule. On the bulk truncated surface the adsorption energy of −2.12 eV per adsorbate is almost twice as high. The distances of the formate species to the octahedral Fe, on the other hand, are comparable with 2.06 Å on the SCV reconstructed surface and 2.03 Å on the bulk truncated surface. Therefore, the difference in adsorption energies is mainly attributed to the dissociated hydrogen atoms rather than to a stronger binding of the formate. The magnetic moments of the surface iron atoms change by only less than 0.1 μ_B due to adsorption. A comparison of the "tet" and "int" adsorption sites yields a slight preference for the "tet" site of approximately 0.04 eV per adsorbed molecule at both the SCV reconstructed and the bulk truncated surface. This small energy difference explains the mixture of adsorption positions observed in the SXRD experiments performed at room temperature. Apart from the adsorption site, the adsorption energy also depends significantly on the positions of the hydrogen atoms stemming from the dissociation of the carboxylic group of the formic acid upon adsorption. The energies given above were calculated for the dissociated hydrogen sitting at the oxygen atoms next to "int" Fe positions in the surface layer, which are empty for the bulk truncated surface while half of them are occupied for the SCV reconstructed surface (Fig. 2b).

If the hydrogen atom, however, is positioned at an oxygen atom next to a tetrahedral iron atom, the adsorption is less favorable by 0.47 eV per adsorbed formic acid molecule at the bulk truncated surface. This is consistent with a first-principles studies on atomic hydrogen and dissociative water adsorption at the Fe_3O_4(001) surface, in which the hydrogen atoms are found to occupy the interstitial gaps first[13,16,19]. In principle, for a SCV reconstructed surface cell there are 28 possibilities to position the two dissociated hydrogen atoms at the eight surface oxygen atoms. Considering only possibilities with hydrogen at the interstitial gaps and taking into account the symmetry of the surface unit cell, there are still two different configurations left, namely the positioning at two different interstitial gaps and the positioning on opposite sides of the same interstitial gap. As expected, the positioning at two different gaps is slightly more favorable by $\Delta E = 0.12$ eV per adsorbed molecule, because of the Coulomb repulsion between the positively charged hydrogen atoms. Another possibility is that the dissociated hydrogen atoms may occupy the octahedral iron vacancies of the reconstructed surface. But, during structural energy minimization of such configurations the hydrogen always relaxed back to the position on top of the surface. So this possibility can be ruled out as it is energetically not favorable.

There is an excellent agreement between the atomic positions of the bulk truncated surface with a full coverage of formic acid adsorbed at the energetically more favorable "tet" site and the results from SXRD after exposure to 50 L formic acid. The deviations are lower than 0.1 Å for almost all positions, see Supplementary Table 2 for comparison. Only some of the oxygen positions deviate up to 0.17 Å. These slight deviations may be explained by the larger fitting error for the less strongly scattering oxygen ions and the fact that in the SXRD model both adsorption sites are included.

The difference in adsorption energy between the SCV reconstructed and the bulk truncated surface already indicates a stabilization of the bulk truncated surface by formic acid. This can be seen more quantitatively in the surface phase diagram in Fig. 3. There, the most stable surface structures in terms of the surface energy are shown for different chemical potentials of the oxygen and formic acid gas reservoirs. The chemical potentials can be converted to experimental conditions, namely temperature

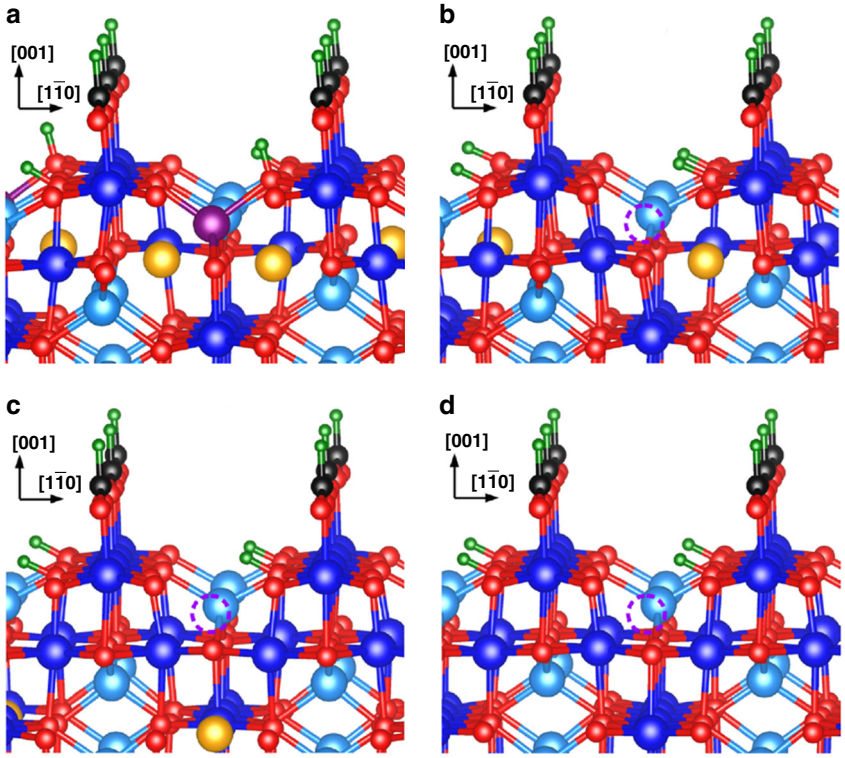

Fig. 4 Surface reconstruction lifting mechanism. **a** Reconstructed surface. **b** The interstitial Fe (violet) hopped to a neighboring octahedral vacancy (orange). **c** The other octahedral vacancy was filled with an octahedral Fe atom (dark blue) from the layer below. **d** Bulk truncated surface

and pressure of the gas phase, assuming validity of the ideal gas equation and an ideal gas mixture[20] using thermochemistry data[21,22]. For formic acid also the formation of a dimer configuration at higher pressures has to be considered[22]. A detailed description of this conversion is given in the Supplementary Methods, conversion of chemical potentials to pressure scales.

At low formic acid chemical potential (lower part in Fig. 3) the reconstructed surface is most stable even at low oxygen chemical potentials. With increasing formic acid pressure and chemical potential, the bulk truncation gets more stable. The stabilization of the bulk truncation is highest at full coverage of formic acid. But for higher oxygen chemical potentials (upper right corner in Fig. 3) one would still expect the reconstructed surface to be more stable because of the higher oxidation state of the surface. However, searching for possible transition structures between the SCV reconstructed and the bulk truncated surface, we found that a bulk truncation with an additional bulk vacancy (see Fig. 4c) is more stable than the reconstructed surface at full formic acid coverage, which will be discussed in the following paragraph. In conclusion, the DFT calculations and the derived surface phase diagram in Fig. 3 predict that the bulk truncated structure is thermodynamically most stable over the whole range of oxygen chemical potentials when the magnetite (001) surface is fully covered by formic acid. This agrees very well with the experiments, where this surface structure is also observed as discussed above.

Reconstruction lifing mechanism. Since the SCV reconstructed surface is iron deficient compared to the bulk truncated surface, the question arises where the additional iron comes from to lift the reconstruction. In order to answer this question, the energies of two possible transition structures, which are shown in Fig. 4, were calculated. Both transition structures are lower in energy than the SCV reconstructed surface (Fig. 4a) at full coverage. The first one (Fig. 4b), where one subsurface vacancy is filled with the interstitial iron, is more stable by 47 meV per unit cell. Even more stable by 130 meV per unit cell compared to the reconstructed surface is the second structure (Fig. 4c), where both subsurface vacancies are filled with the interstitial iron and some bulk iron leaving behind a bulk vacancy. Since the stoichiometry of this bulk truncated surface with a bulk vacancy is the same as for the reconstructed surface, the former is more stable independent of the oxygen chemical potential. Therefore, in the surface phase diagram (Fig. 3) no reconstructed surface with full coverage (shown in Fig. 4a) is present. It is thus plausible from an energetic point of view that the additional iron stems from the bulk and diffuses to the surface. The diffusion path and barriers, however, are not investigated here.

In a computational study the diffusion barrier for iron hopping from one octahedral site to a neighboring octahedral vacancy in the bulk was calculated to be 0.70 eV[23]. The diffusion barrier between an interstitial tetrahedral iron atom and a neighboring octahedral vacancy was only 0.05 eV. Therefore, we argue that the lifting of the surface reconstruction starts with the diffusion of the surface tetrahedral interstitial iron ion to the underlying octahedral vacancies. Then, in a second step, octahedral iron from the bulk can fill the remaining subsurface vacancies. On the other hand, the diffusion paths and barriers might deviate from the bulk values because of the proximity to the surface and the energy gain in the different steps as described above. Surface strain may be present and can influence diffusion barriers as well. In addition, the structures described here do not cover the space of possible intermediate structures exhaustively, so more complex sub-steps might play a role during the transition. The energy gain due to adsorption and from lifting the reconstruction might

trigger the near surface diffusion process, but further studies are needed to address this point more elaborately.

Theoretical assessment of molecular vibrational modes. In the last part of the results, we will compare calculated and experimental infrared (IR) spectra of formic acid on magnetite (001). The calculated vibrational spectrum of formic acid adsorbed at the bulk truncated magnetite (001) surface for both the "tet" and "int" adsorption sites are shown in Fig. 5 together with the experimental data. The symmetric and asymmetric O–C–O stretch modes at 1368 and 1544 cm^{-1} in the experimental data in Fig. 5a) exhibit a Fano type line shape, characteristic for the adsorption on materials like Fe_3O_4[12], which exhibits a dielectric response between a perfect conductor and a perfect dielectric. The band from symmetric vibrations is probed by electric field components of the unpolarized beam perpendicular to the surface, whereas the band from asymmetric vibrations is probed by electric field components parallel to the surface[8]. If the electric field component parallel to the surface of "p" polarized photons dominates over "s" polarized photons, the sign of the IR signal is inverted, as observed for the asymmetric stretch band at 1544 cm^{-1} [8,24]. Similarly, the C–H bending mode at 1383 cm^{-1} exhibits a transition dipole moment parallel to the surface, which is excited by the s polarized and the p polarized component parallel to the surface, resulting also in an inverted Fano line shape, as compared to the symmetric stretch band.

There is a large difference in the O–C–O stretching modes in the range from 1000 to 2000 cm^{-1} as compared to the calculated gas phase spectrum (see Supplementary Fig. 4 and Supplementary Table 5, together with an overview of all calculated IR spectra), due to the dissociation of the carboxyl group upon adsorption. The band positions for the "tet" adsorption site (see Fig. 5b) fit well to the experimental IR spectra considering that there is a small systematic shift of calculated vibrational frequencies because of the harmonic and density-functional approximations[25–27]. The theoretical asymmetric stretch band is shifted to lower waves numbers by 14 cm^{-1} and the shift amounts to 30 cm^{-1} for the symmetric stretch band. The theoretical splitting is with 208 cm^{-1} larger than the experimental value (176 cm^{-1}). A similar trend was also observed for formic acid on ZnO($10\bar{1}0$)[24]. The theoretical spectrum of formic acid on the "int" adsorption site (Fig. 5c) is found to be shifted by 4 cm^{-1} to lower wave numbers, in line with its slightly lower binding energy. A closer inspection of the FT-IRRAS data indeed confirms the presence of a component red shifted by a few wave numbers, and a small amplitude, in line with the 10% occupancy of the "int" site identified in the SXRD analysis. Further on, the C–H bending mode is theoretically predicted at 1343 cm^{-1}, in good agreement with the experimental results (1383 cm^{-1}).

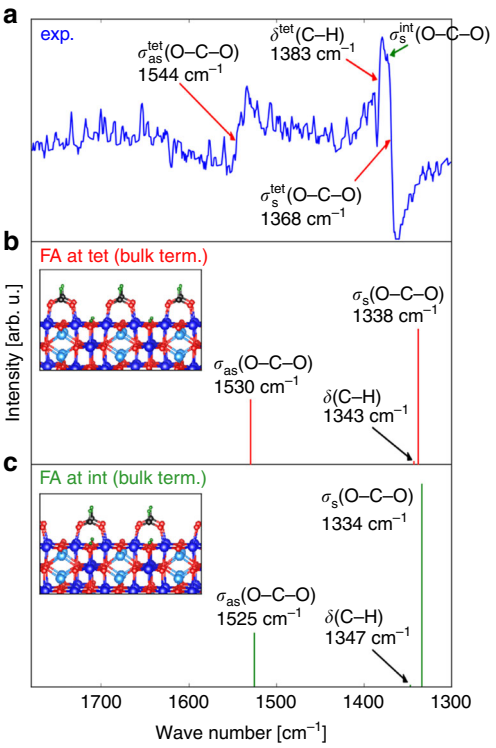

Fig. 5 Infrared spectroscopy results. **a** Experimental FT-IRRAS spectrum from formic acid on Fe_3O_4(001). Calculated vibrational spectra of formic acid adsorbed at the bulk truncated surface in "tet" (**b**) and "int" site (**c**). In the insets in (**b**), and (**c**), the adsorption geometries are presented

Discussion

We have determined the atomic structure of the formic acid/magnetite (001) interface by a combination of surface X-ray diffraction and density functional theory. We consistently found that the majority of formate molecules adsorb in bidentate geometry on octahedrally coordinated Fe ion rows, centered around adjacent tetrahedally coordinated Fe ions ("tet" sites). Hydrogen released during the dissociative formic acid adsorption at room temperature further stabilizes the unreconstructed magnetite (001) surface as compared to the SCV reconstructed surface. We found that the formic acid adsorption induced lifting of the SCV reconstruction is accompanied by significant atomic relaxations back to their bulk positions. By a combination of SXRD and DFT results, we identified the atomistic SCV reconstruction lifting mechanism as the following: We propose that it proceeds by a filling of one of the subsurface octahedral vacancies per unit cell by Fe ions from tetrahedral interstitial sites at the surface of the SCV structure. The SXRD structural analysis demonstrates that the second subsurface octahedral vacancy is also occupied during the reconstruction lifting process. The DFT calculations give further evidence that formic acid adsorption induced transient structures of the bulk truncated surface with deeper layer subsurface Fe vacancies are more stable than the formic acid covered SCV reconstructed surface. This is in line with a dissolution of a cation vacancy in the bulk at room temperature, which is calculated to be a thermodynamically stable configuration. We propose that a similar mechanism gets activated during the atomic hydrogen and water induced lifting of the reconstruction. The IR spectra calculated by DFT are in quantitative agreement with the experimental FT-IRRAS spectra and confirm the interpretation of the IR results in line with a dissociation of formic acid upon adsorption in bidentate geometry. Our results demonstrate that the adsorption of carboxylic acids on oxide surfaces can alter their near surface stoichiometry. The experiments and calculations give evidence that magnetite exhibits a high near surface cation mobility, even at room temperature, which is expected to have strong impact on catalytic reactions involving alternating reducing and oxidizing conditions or on the binding of longer chain organic molecules, such as oleic acid. Tailoring the strength of the organic/oxide interface may have large impact on the design of novel hierarchical materials composed of nanometric oxide/organic building blocks.

Methods

Experimental methods. Surface X-ray diffraction experiments were performed at the ID03-beamline at the European Synchrotron Radiation Facility (ESRF)[28] at a photon energy of 14 keV using a 2D-detector in stationary mode[29]. The (001) surface of a natural magnetite single crystal was cleaned in UHV at a base pressure of 1×10^{-10} mbar by multiple cycles of sputtering with 1 keV Ar^+ ions and

annealing at 923 K. This results in a reconstructed, chemically clean surface, as confirmed by x-ray photoelectron spectroscopy at the DESY NanoLab[30], see Supplementary Fig. 5. Formic acid (>98% purity) was further cleaned by repeated freeze-pump-thaw cycles. It was dosed at room temperature through a leak valve into the chamber at a pressure of 5×10^{-8} mbar. SXRD data sets were recorded from the clean surface and after exposure to 10 and 50 L of formic acid, respectively. The SXRD data was analyzed utilizing the program package ANAROD[18]. The relative reciprocal lattice coordinates (H,K,L) are given in units of $\frac{2\pi}{a}$, with bulk lattice parameter of magnetite of $a = 8.394$ Å. FT-IRRAS measurements were performed in a high resolution IR spectrometer coupled to an UHV chamber (base pressure 5×10^{-10} mbar) via differentially pumped KBr windows[30]. Each IR spectrum was accumulated in 1024 scans with a resolution of 1 cm^{-1} and was recorded with an unpolarized beam at 80° incidence angle as a function of the formic acid exposure.

Computational methods. Calculations based on density functional theory (DFT) were performed with the plane wave code VASP[31,32] and results for the functionals PBE[33] and optB86b-vdW[34,35] were compared. However, since the inclusion of van-der-Waals interactions changed the adsorption energies by only approximately 0.2 eV per formic acid molecule and yielded the same qualitative results, here only the results for the PBE functional are shown and discussed while the results for the optB86b-vdW functional can be found in the Supplementary Information (SI). For all calculations an on-site Coulomb potential with the Hubbard parameter $U_{eff} = 4.0$ eV was added using the approach by Duradev et al.[36] to account for the correlation of the d-electrons at the Fe atoms. Past studies have shown that this choice of PBE + U reproduces the energetic ordering of iron oxide structures well even though more accurate hybrid functionals are needed for the calculation of accurate formation enthalpies[37,38]. After relaxation of the atomic positions of Fe, O, C, and H, as well as determination of the electronic ground state, vibrational spectra were calculated using density-functional perturbation theory (DFPT) and Born effective charges[39–43]. A more detailed description of the computational settings can be found in the Supplementary Methods, computational details.

Data availability

All relevant data are available from the authors.

Received: 30 April 2019 Accepted: 16 July 2019
Published online: 09 August 2019

References

1. Baeza, A., Guillena, G. & Ramón, D. J. Magnetite and metal-impregnated magnetite catalysts in organic synthesis: A very old concept with new promising perspective. *ChemCatChem* **8**, 49–67 (2016).
2. Zhu, M. & Wachs, I. E. Iron-based catalysts for the high-temperature water–gas shift (HT-WGS) reaction: a review. *ACS Catal.* **6**, 722–732 (2016).
3. Cho, J. M., Jeong, M. H. & Bae, J. W. Fischer-Tropsch synthesis on potassium-modified Fe_3O_4 nanoparticles. *Res. Chem. Intermed.* **42**, 335–350 (2016).
4. Pacholski, C., Kornowski, A. & Weller, H. Self–assembly of ZnO: From nanodots to nanorods. *Angew. Chem. Int. Ed.* **41**, 1188–1191 (2002).
5. Zhang, L., He, R. & Gu, H.-C. Oleic acid coating on the monodisperse magnetite nanoparticles. *Appl. Surf. Sci.* **253**, 2611–2617 (2006).
6. Dreyer, A. et al. Organically linked iron oxide nanoparticle supercrystals with exceptional isotropic mechanical properties. *Nat. Mater.* **15**, 522–528 (2016).
7. Domènech, B. et al. Hierarchical supercrystalline nanocomposites through the self-assembly of organically-modified ceramic nanoparticles. *Sci. Rep.* **9**, 3435 1–11 (2019).
8. Wang, Y. & Wöll, C. IR spectroscopic investigations of chemical and photochemical reactions on metal oxides: bridging the materials gap. *Chem. Soc. Rev.* **46**, 1875–1932 (2017).
9. Parkinson, G. S. Iron oxide surfaces. *Surf. Sci. Rep.* **71**, 272–365 (2016).
10. Bliem, R. et al. Subsurface cation vacancy stabilization of the magnetite (001). *Surf. Sci.* **346**, 1215–1218 (2014).
11. Arndt, B. et al. Atomic structure and stability of magnetite Fe_3O_4(001): An X-ray view. *Surf. Sci.* **653**, 76–81 (2016).
12. Gamba, O. et al. Adsorption of formic acid on the Fe_3O_4 (001) surface. *J. Phys. Chem. C.* **119**, 20459–20465 (2015).
13. Parkinson, G. S. et al. Semiconductor–half metal transition at the Fe_3O_4(001) surface upon hydrogen adsorption. *Phys. Rev. B* **82**, 125413 (2010).
14. Mulakaluri, N., Pentcheva, R., Wieland, M., Moritz, W. & Scheffler, M. Partial dissociation of water on Fe_3O_4(001): Adsorbate induced charge and orbital order. *Phys. Rev. Lett.* **103**, 176102 (2009).
15. Meier, M. et al. Water agglomerates on Fe_3O_4(001). *Proc. Natl Acad. Sci.* **115**, E5642–E5650 (2018).
16. Liu, H. & Di Valentin, C. Bulk-terminated or reconstructed Fe_3O_4(001) surface: water makes a difference. *Nanoscale* **10**, 11021–11027 (2018).
17. Sayago, D. I. et al. Structure determination of formic acid reaction products on TiO_2 (110). *J. Phys. Chem. B* **108**, 14316–14323 (2004).
18. Vlieg, E. ROD: a program for surface X-ray crystallography. *J. Appl. Crystallogr.* **33**, 401–405 (2000).
19. Mulakaluri, N. & Pentcheva, R. Hydrogen adsorption and site-selective reduction of the Fe_3O_4(001) surface: Insights from first principles. *J. Phys. Chem. C.* **116**, 16447–16453 (2012).
20. Reuter, K. & Scheffler, M. Composition, structure, and stability of RuO_2 (110) as a function of oxygen pressure. *Phys. Rev. B* **65**, 035406 (2001).
21. Chase, M. W. NIST-JANAF thermochemical tables 4th edn, In *NIST-JANAF Thermochemical Tables 2 Volume-Set* (American Chemical Society and American Institute of Physics, Gaithersburg, MD, 1998).
22. Chao, J. & Zwolinski, B. J. Ideal gas thermodynamic properties of methanoic and ethanoic acids. *J. Phys. Chem. Ref. Data* **7**, 363–377 (1978).
23. Muhich, C. L., Aston, V. J., Trottier, R. M., Weimer, A. W. & Musgrave, C. B. First-Principles Analysis of Cation Diffusion in Mixed Metal Ferrite Spinels. *Chem. Mater.* **28**, 214–226 (2016).
24. Buchholz, M. et al. The Interaction of Formic Acid with Zinc Oxide: A Combined Experimental and Theoretical Study on Single Crystal and Powder Samples. *Top. Catal.* **58**, 174–183 (2015).
25. Li, X. & Paier, J. Adsorption of Water on the Fe_3O_4(111) Surface: Structures, Stabilities, and Vibrational Properties Studied by Density Functional Theory. *J. Phys. Chem. C.* **120**, 1056–1065 (2016).
26. Li, X. et al. Surface Termination of Fe_3O_4(111) Films Studied by CO Adsorption Revisited. *J. Phys. Chem. B* **122**, 527–533 (2018).
27. Würger, T. et al. Adsorption of acetone on rutile TiO_2: A DFT and FTIRS study. *J. Phys. Chem. C.* **122**, 19481–19490 (2018).
28. Balmes, O. et al. The ID03 surface diffraction beamline for in-situ and real-time X-ray investigations of catalytic reactions at surfaces. *Catal. Today* **145**, 220–226 (2009).
29. Schlepütz, C. M. et al. Improved data acquisition in grazing-incidence x-ray scattering experiments using a pixel detector. *Acta Crystallogr. Sect. A: Found. Crystallogr.* **61**, 418–425 (2005).
30. Stierle, A., Keller, T. F., Noei, H., Vonk, V. & Roehlsberger, R. Desy nanolab. *J. Large-Scale Res. Facil. JLSRF* **2**, 76 (2016).
31. Kresse, G. & Furthmüller, J. Efficient iterative schemes for ab initio total-energy calculations using a plane-wave basis set. *Phys. Rev. B* **54**, 11169–11186 (1996).
32. Kresse, G. & Furthmüller, J. Efficiency of ab-initio total energy calculations for metals and semiconductors using a plane-wave basis set. *Comput. Mater. Sci.* **6**, 15–50 (1996).
33. Perdew, J. P., Burke, K. & Ernzerhof, M. Generalized gradient approximation made simple. *Phys. Rev. Lett.* **77**, 3865–3868 (1996).
34. Klimeš, J., Bowler, D. R. & Michaelides, A. Chemical accuracy for the van der Waals density functional. *J. Phys.: Condens. Matter* **22**, 022201 (2010).
35. Klimeš, J., Bowler, D. R. & Michaelides, A. Van der Waals density functionals applied to solids. *Phys. Rev. B* **83**, 195131 (2011).
36. Dudarev, S. L., Botton, G. A., Savrasov, S. Y., Humphreys, C. J. & Sutton, A. P. Electron-energy-loss spectra and the structural stability of nickel oxide: An LSDA + U study. *Phys. Rev. B* **57**, 1505–1509 (1998).
37. Guo, H., & Barnard, A. S. Modeling the iron oxides and oxyhydroxides for the prediction of environmentally sensitive phase transformations. *Phys. Rev.* **83**, 194112 (2011).
38. Meng, Y. et al. When density functional approximations meet iron oxides. *J. Chem. Theory Comput.* **12**, 5132–5144 (2016).
39. Baroni, S., Giannozzi, P. & Testa, A. Green's-function approach to linear response in solids. *Phys. Rev. Lett.* **58**, 1861–1864 (1987).
40. Gonze, X. Perturbation expansion of variational principles at arbitrary order. *Phys. Rev. A* **52**, 1086–1095 (1995).
41. Giannozzi, P. & Baroni, S. Vibrational and dielectric properties of C_{60} from density–functional perturbation theory. *J. Chem. Phys.* **100**, 8537–8539 (1994).
42. Giannozzi, P. & Baroni, S. Density-functional perturbation theory. In *Handbook of Materials Modeling*. 195–214 (Springer, Dordrecht, 2005).
43. Karhánek, D., Bučko, T. & Hafner, J. A density-functional study of the adsorption of methane-thiol on the (111) surfaces of the Ni-group metals: II. Vibrational spectroscopy. *J. Phys. Condens. Matter* **22**, 265006 (2010).

Acknowledgements

The authors thank Ulrike Diebold, Gareth Parkinson, and Michael Schmid for fruitful discussions. This work was funded by the Deutsche Forschungsgemeinschaft (DFG, German Research Foundation)–Projektnummer 192346071–SFB 986.

Author contributions

B.A. and K.S. wrote the paper together with A.S. and G.F.; B.A., E.G., K.K., M.C. and V.V. performed the x-ray diffraction experiment. M.C. and H.N. performed the infrared reflection absorption spectroscopy experiment. K.S., G.F. and S.M. performed the

theoretical calculations. G.F. supervised the computational work. A.S. developed the experimental idea.

Additional information

Supplementary information accompanies this paper at https://doi.org/10.1038/s42004-019-0197-1.

Competing interests: The authors declare no competing interests.

Reprints and permission information is available online at http://npg.nature.com/reprintsandpermissions/

Publisher's note: Springer Nature remains neutral with regard to jurisdictional claims in published maps and institutional affiliations.